Monthly Notices of the ROYAL ASTRONOMICAL SOCIETY

MNRAS **532,** 1887–1900 (2024) https://doi.org/10.1093/mnras/stae1618
Advance Access publication 2024 July 01

Measuring the ejecta velocities of type Ia supernovae from the pan-STARRS1 medium deep survey

Y.-C. Pan [1]★ Y.-S. Jheng,[1] D. O. Jones,[2] I.-Y. Lee,[1] R. J. Foley,[3] R. Chornock [4] D. M. Scolnic [5] E. Berger,[6] P. M. Challis,[6] M. Drout,[7] M. E. Huber [8] R. P. Kirshner,[6] R. Kotak,[9] R. Lunnan,[10] G. Narayan,[11] A. Rest,[12,13] S. Rodney[14] and S. Smartt[15]

[1]*Graduate Institute of Astronomy, National Central University, 300 Jhongda Road, 32001 Jhongli, Taiwan*
[2]*Gemini Observatory, NSF's NOIRLab, 670 N. A'ohoku Place, Hilo, Hawai'i, 96720, USA*
[3]*Department of Astronomy and Astrophysics, University of California, Santa Cruz, CA 92064, USA*
[4]*Department of Astronomy, University of California, Berkeley, CA 94720-3411, USA*
[5]*Department of Physics, Duke University, Durham, NC 27708, USA*
[6]*Center for Astrophysics, Harvard & Smithsonian, Cambridge, MA 02138, USA*
[7]*Department of Astronomy and Astrophysics, University of Toronto, 50 St. George St., Toronto, Ontario, M5S 3H4, Canada*
[8]*Institute for Astronomy, University of Hawaii, 2680 Woodlawn Drive, Honolulu, HI 96822, USA*
[9]*Department of Physics and Astronomy, University of Turku, FI-20014 Turku, Finland*
[10]*Department of Astronomy, The Oskar Klein Centre, Stockholm University, AlbaNova, SE-106 91 Stockholm, Sweden*
[11]*Department of Astronomy, University of Illinois at Urbana-Champaign, Urbana, IL 61801, USA*
[12]*Department of Physics and Astronomy, Johns Hopkins University, 3400 North Charles Street, Baltimore, MD 21218, USA*
[13]*Space Telescope Science Institute, 3700 San Martin Drive, Baltimore, MD 21218, USA*
[14]*Department of Physics and Astronomy, University of South Carolina, 712 Main St., Columbia, SC 29208, USA*
[15]*Astrophysics Research Centre, School of Mathematics and Physics, Queen's University, Belfast BT7 1NN, UK*

Accepted 2024 June 27. Received 2024 June 22; in original form 2024 February 15

ABSTRACT

There is growing evidence that Type Ia supernovae (SNe Ia) may originate from multiple explosion channels. Previous studies have indicated that the ejecta velocity of SNe Ia is one powerful tool to discriminate between different channels. In this work, we study ∼400 confirmed SNe Ia discovered by the Pan-STARRS1 Medium Deep Survey (PS1-MDS), and obtain a sample of ∼50 SNe Ia that have near-peak Si II λ6355 velocity ($v_{\rm Si\,II}$) measurements. We investigate the relationships between $v_{\rm Si\,II}$ and various parameters, including SN light-curve width, colour, host galaxy properties, and redshift. No significant trends are identified between $v_{\rm Si\,II}$ and light-curve parameters. Regarding the host-galaxy properties, we see a significant trend that high-velocity (HV) SNe Ia ($v_{\rm Si\,II} \gtrsim 12000$ km s^{-1}) tend to reside in more massive galaxies compared to normal velocity (NV) SNe Ia ($v_{\rm Si\,II} < 12000$ km s^{-1}) when combining both the PS1-MDS data set and those from previous low-z studies. While we do not see a significant trend between $v_{\rm Si\,II}$ and redshift, HV SNe Ia appear to be more prevalent in low-z samples than in high-z samples. We discuss several possibilities that could potentially contribute to this trend. Furthermore, we investigate the potential bias on SN Ia distances and find no significant difference in Hubble residuals between HV and NV subgroups.

Key words: transients: supernovae.

1 INTRODUCTION

Type Ia supernovae (SNe Ia) are mature standardizable candles that are frequently used to measure the cosmological parameters (e.g. Riess et al. 1998, 2007; Perlmutter et al. 1999; Kessler et al. 2009; Sullivan et al. 2011; Suzuki et al. 2012; Scolnic et al. 2018; Abbott et al. 2019; Jones et al. 2019; Brout et al. 2022). These studies generally assumed that the SNe Ia originated from a uniform class and showed negligible evolution over the cosmological time. In practice, we do not fully understand these exceptional explosions, such as their progenitor system and the explosion mechanism. Thus, the degree to which SN Ia properties change with redshift and how that will impact the precision of the cosmological parameters will become an important consideration in their future use.

Previous studies have shown some evidence that SN Ia properties could change with redshift. Howell et al. (2007) first studied the light-curve width as a function of redshift. After carefully selecting their sample to minimize the Malmquist bias, they found SNe Ia at higher redshift tend to have a wider light-curve width. This further implies that the higher-z SNe Ia are on average brighter than the lower-z SNe Ia (based on the width and luminosity relation; Phillips 1993). This trend has also been confirmed by Nicolas et al. (2021) with a more recent data set.

★ E-mail: ycpan@astro.ncu.edu.tw

The SN Ia spectral features as a function of redshift were also investigated by several studies. Bronder et al. (2008) studied three spectral features (Ca II H&K, Si II λ4000, and Mg II) and found that the low-z and high-z samples are generally similar except for the equivalent width (EW) of Mg II line. In contrast, Walker et al. (2011) did not see a significant difference in the EW of Mg II between the low-z and high-z samples; however, they found the strength of Si II λ4000 decreases with redshift. Foley et al. (2008) constructed the SN Ia composite spectra based on the redshift. Their results revealed an ultraviolet (UV) excess for the composite spectrum of the high-z sample, also a significant difference in the strength of Fe III λ5129 between low-z and high-z composite spectra. The trend that higher z SNe Ia tend to have a UV excess has also been confirmed by Balland et al. (2018). In addition, the results from Sullivan et al. (2009) and Balland et al. (2009) both indicated that the higher z SNe Ia tend to show lower intermediate-mass element (IME) abundances than that of lower z counterparts, although Sullivan et al. (2009) attributed this trend as changes in SN Ia demographics rather than the evolution of photometrically similar SNe.

Most studies mentioned above could not investigate the SN spectral properties redward of 6000 Å (e.g. the Si II λ6355 line) due to the limited wavelength coverage at high-redshift. Foley (2012) was the first to look into the relation between Si II λ6355 velocity ($v_{\rm Si\,II}$) and redshift, but they found an insignificant difference in $v_{\rm Si\,II}$ between low-z and high-z SNe Ia with a small sample. More recent studies suggested that SN Ia ejecta velocity is likely to correlate with the host galaxy environment. For example high-velocity (HV) SNe Ia ($v_{\rm Si\,II} \gtrsim 12000$ km s^{-1}; Wang et al. 2009) tend to reside in more massive galaxies than their normal-velocity (NV; $v_{\rm Si\,II} \lesssim 12000$ km s^{-1}) counterparts (Pan et al. 2015; Pan 2020; Dettman et al. 2021). Considering the evolution of galaxy populations, Pan (2020) suspected that the fraction of HV SN Ia may decrease with redshift. With a new light-curve model, Jones et al. (2022) found a marginal trend that SNe Ia tend to have larger Si II λ6355 EWs in low-mass galaxies, but they did not see a trend with $v_{\rm Si\,II}$.

Wang et al. (2009) proposed that HV SNe Ia are likely to have a different origin from NV SNe Ia, given their preference for a lower extinction ratio (R_V) than that of NV SNe Ia. There is also evidence that the HV SNe Ia tend to show a blue excess in their late-time light curves and variable Na I absorption lines in their spectra (Wang et al. 2019). In addition to their preference for massive host galaxies (e.g. Pan et al. 2015; Pan 2020), they also tend to be more concentrated in the inner regions of their host galaxies, whereas the NV events span a wider range of radial distances (Wang et al. 2013). In the nebular phase, a few studies have indicated that HV SNe Ia tend to show redshifted [Fe II λ7155] line, while NV SNe Ia could have either blueshifted or redshifted [Fe II λ7155] line in their spectra (Maeda et al. 2010; Maguire et al. 2018; Li et al. 2021). This trend implies that HV SNe Ia (and at least part of the NV SNe Ia) could be produced via asymmetric explosions. It is not yet clear if the HV and NV SNe Ia are physically distinct and produced via different channels. Theoretical studies proposed that the sub-Chandrasekhar-mass WD explosions could be a promising mechanism to explain the wide range of $v_{\rm Si\,II}$ (including the HV SNe Ia) as found by spectroscopic observations (e.g. Polin, Nugent & Kasen 2019; Shen et al. 2021). The simulation of sub-Chandrasekhar-mass explosions from these studies are generally consistent with the observational properties of HV SNe Ia, such as their unique colour and ejecta velocity. However, more precise physics, radiative transfer, and the effect of secondary star (e.g. Pakmor et al. 2022) need to be considered in future works.

Motivated by the growing evidence that SNe Ia are likely to result from multiple channels, and that their ejecta velocities could be key to distinguishing between different channels of explosion, we measure the ejecta velocity from the Si II λ6355 absorption line of the SNe Ia discovered by the Pan-STARRS1 Medium Deep Survey (PS1-MDS) in this paper. We aim to investigate the relations between $v_{\rm Si\,II}$ and several SN and host galaxy properties, and compare them with low-z studies. A plan of this paper follows. In Section 2, we discuss our SN Ia spectroscopic sample, $v_{\rm Si\,II}$ measurement, and the determination of host-galaxy parameters. The results are shown in Section 3. The discussion and conclusions are presented in Sections 4 and 5, respectively. Throughout this paper, we assume $H_0 = 70$ km s^{-1} Mpc^{-1} and a flat universe with $\Omega_M = 0.3$ if not mentioned otherwise.

2 DATA AND METHOD

2.1 Spectroscopic observations of PS1-MDS SNe

Here, we study the spectroscopically confirmed SNe Ia discovered by the PS1-MDS. The details of the PS1-MDS and its selection process can be found in Rest et al. (2014) and Scolnic et al. (2018). The spectroscopic observations were obtained with a variety of telescope/instrument combinations, including the FAST Spectrograph on the 1.5-m Tillinghast Telescope (Fabricant et al. 1998), the Supernova Integrated Field Spectrograph (SNIFS; Aldering & Supernova Factory 2007) on the University of Hawai'i 88-inch (UH88) telescope, the Alhambra Faint Object Spectrograph and Camera (ALFOSC) on the 2.56-m Nordic Optical Telescope, the Dual Imaging Spectrograph (DIS) on the Astrophysical Research Consortium 3.5-m Telescope, the Ritchey–Chretien Spectrograph on the Kitt Peak National Observatory 4-m telescope, the Intermediate dispersion Spectrograph and Image System (ISIS) on the 4.2-m William Herschel Telescope (WHT), the Blue Channel Spectrograph (Schmidt, Weymann & Foltz 1989) and Hectospec (Fabricant et al. 2005) on the 6.5-m Multiple Mirror Telescope (MMT), the Low Dispersion Survey Spectrograph-3 (LDSS3) and the Magellan Echellette (MagE; Marshall et al. 2008) on the 6.5-m Magellan Clay telescope, the Inamori–Magellan Areal Camera and Spectrograph (IMACS; Dressler et al. 2011) on the 6.5-m Magellan Baade telescope, the Gemini Multi-Object Spectrographs (GMOS; Hook et al. 2004) on both 8.1-m Gemini North and South telescopes, the DEep Imaging Multi-Object Spectrograph (DEIMOS) on the 10-m Keck-II telescope (Faber et al. 2003), and the Optical System for Imaging and low-Intermediate-Resolution Integrated Spectroscopy (OSIRIS; Cepa et al. 2003) on the 10.4-m Gran Telescopio CANARIAS (GTC).

The spectra are reduced with IRAF[1] and Interactive Data Language (IDL) tasks following the standard procedure (bias subtraction, flat-fielding, wavelength calibration, and flux calibration). When possible, we carefully select the background regions to subtract the host-galaxy light when extracting the 1D spectrum. This can help reduce the host-galaxy contamination on the SN spectra. A summary of spectroscopic observation for all the confirmed SNe Ia can be found in Table 1, and their spectra are available from the WISeREP archive (Yaron & Gal-Yam 2012).

[1]The Image Reduction and Analysis Facility (IRAF) is distributed by the National Optical Astronomy Observatories, which are operated by the Association of Universities for Research in Astronomy, Inc., under a cooperative agreement with the National Science Foundation.

Table 1. Summary of spectroscopically confirmed SN Ia in this work. The entire table is available online as supplementary material. A portion is shown here for guidance regarding its form and content.

SN Name	Telescope	MJD	Phase (d)	$z_{\rm CMB}$	z source
PS1-909006	Gemini	55 098	17.1	0.283	host
PS1-909010	Gemini	55 105	6.4	0.276	host
PS1-910016	Gemini	55 125	19.7	0.22	SN
PS1-910017	Gemini	55 125	12.0	0.32	SN
PS1-910018	Gemini	55 125	12.1	0.264	host
PS1-910020	Gemini	55 124	14.3	0.242	host
PS1-910021	Gemini	55 125	20.2	0.256	host
PS1-000006	Magellan	55 216	10.0	0.231	host
PS1-000010	Magellan	55 217	1.7	0.246	host
PS1-000011	Gemini	55 214	2.7	0.381	host

Table 2. The SN sample selection in this work.

	Number of SNe left
Confirmed as SN Ia	381
Redshift derived from host	321
LC quality cut	283
Phase cut	126
With Si II λ6355 measurement	48

2.2 Sample selection

The objects studied in this work were all spectroscopically confirmed as SN Ia. We use the Supernova Identification (SNID; Blondin & Tonry 2007) code to classify the SNe. The classification scheme is briefly summarized as follows: We first clipped or masked the nebular emission lines from the host galaxy (if any) in the spectra before SNID classification. The redshift is forced to be fixed if known (e.g. from the host galaxy). The SNID classification is mainly based on the quality parameter named '*rlap*' (see Blondin & Tonry 2007). The higher *rlap* indicates a better correlation (as weighted by the overlap in wavelength space) between the input spectrum and the template. Following the method in Miknaitis et al. (2007), we classify a supernova to be Ia if its best-match template from SNID is an Ia and at least 50 per cent of the templates with *rlap* larger than 5.0 are also Ia. A total of 362 objects pass the criterion and are confirmed as Ia. We classify another 19 objects as Ia (which fail to pass our SNID criteria) with eye inspection. The final parent sample contains 381 spectroscopically confirmed SNe Ia.

To measure the ejecta velocity, only SNe with host-galaxy redshift available are included. This gives 321 SNe from the parent sample. We also apply the same quality cuts on SN light curves (LCs) as those described in Scolnic et al. (2018) to ensure a precise phase determination of our spectrum. These include the constraints on LC fitting parameters such as reduced χ^2, the LC width (x_1), and peak date ($pkmjd$) uncertainties. A total of 283 SNe Ia pass the LC quality cut and are used as our final spectroscopic sample. The number of SNe left after each cut is shown in Table 2.

The redshift of our final spectroscopic sample ranges from 0.03 to 0.63, with a median redshift of ∼0.3. Most of the SNe have only single-epoch spectroscopic observation, with <10 per cent of our SNe (21 out of 283) having multi-epoch spectra. The distribution of redshift and phase of the spectra used for classification can be found in Fig. 1.

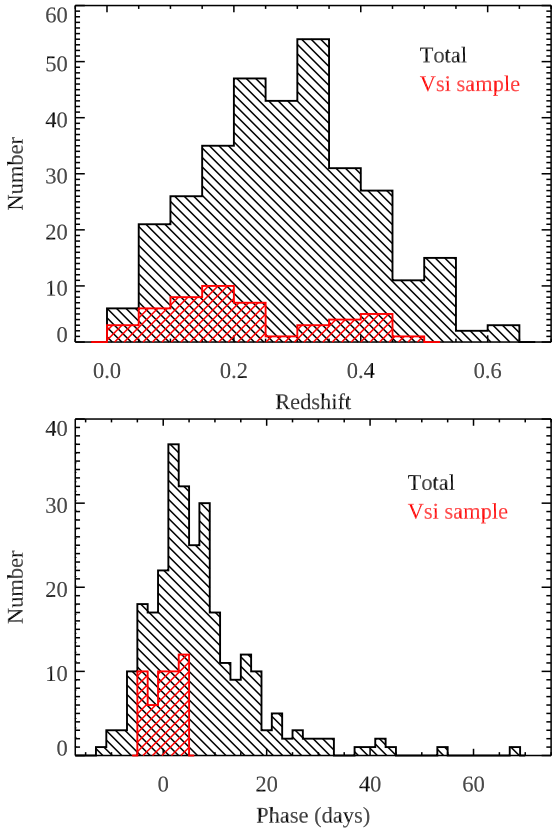

Figure 1. *Upper:* The redshift distributions of our spectroscopic sample (black histogram) and those with $v_{\rm Si\,II}$ measurements available (red histogram). *Lower:* The phase distribution of the spectra we used for classification (black histogram) and those with $v_{\rm Si\,II}$ measurements available (red histogram).

2.3 Si II λ6355 velocity measurement

In this work, we focus on the photospheric velocity measured from the Si II λ6355 line near the maximum light. Si II λ6355 line is selected because it is relatively free from the contamination of other lines and detached high-velocity features (HVFs; Wang et al. 2003; Gerardy et al. 2004; Mazzali et al. 2005) near the maximum light. The alternatives are the Ca II H&K and Ca II NIR lines. However, the Ca II NIR line is not covered by the optical spectrum of our high-z sample. Regarding the Ca II H&K, the existence of HVFs and potential contamination from the Si II λ3858 line could complicate the precise determination of the photospheric component when high-quality spectra are unavailable. (e.g. Foley 2013; Childress et al. 2014; Maguire et al. 2014; Silverman et al. 2015). Given the high-z nature of our data set, we only focus on measuring the Si II λ6355 velocity in this work.

Following Maguire et al. (2014) and Pan et al. (2015), we obtain the near-peak sample by restricting the phase of our spectroscopic observations to be within 5 d relative to the peak luminosity. The velocity evolution within this phase range is expected to be mild and small (e.g. with a mean gradient of ∼ 30 km s^{-1} d^{-1}; Pan et al. 2015). This phase cut gives a near-peak sample of 126 SNe. We further exclude 14 SNe due to the insufficient wavelength coverage on the Si II λ6355 feature. Following Foley (2012), we also perform a visual inspection to exclude the spectra that are noisy and/or have a flat absorption feature, have significant sky residuals, have obvious

reduction issues, or combinations of the above factors. Finally, we are able to measure the $v_{\rm Si\,II}$ from 48 SNe Ia in our sample.

We use the technique from Blondin et al. (2006) to measure the velocity. Following the procedure described in Siebert et al. (2019), the spectrum is first smoothed with an inverse-variance Gaussian kernel of a temporary smoothing factor. An error spectrum is then determined from the smoothed residual spectrum by subtracting the initially smoothed spectrum from the original spectrum. An signal-to-noise ratio (S/N) is estimated using the median flux ratio between the smoothed and the error spectrum. This S/N will be used to determine the final smoothing factor (by adopting the empirical relation in Siebert et al. 2019) to smooth the SN spectrum. The $v_{\rm Si\,II}$ is calculated by measuring the wavelength at the minimum flux of the smoothed Si II λ6355 line. The uncertainties in $v_{\rm Si\,II}$ are estimated by randomly varying the smoothing factor 10 000 times within the typical range of our sample (0.002 to 0.0045). It is noted that the uncertainties in $v_{\rm Si\,II}$ are not considered when classifying our SNe into the HV and NV subgroups. However, we find that this has a negligible effect on our results.

The majority of SNe in our final sample has only a single near-peak spectrum, with two SNe (PS1-350083 and PS1-510266) having multiple near-peak spectra. For the two near-peak spectra of PS1-350083, we adopt the one nearest to the SN maximum light. For PS1-510266, there are also two near-peak spectra, but only one has Si II λ6355 available. The median $v_{\rm Si\,II}$ of our sample is 10923 km s^{-1}, with a minimum and maximum velocity of 9015 and 13459 km s^{-1}, respectively. The redshift distribution of our $v_{\rm Si\,II}$ sample can be found in Fig. 1. Figs A1 and A2 show the observed and smoothed flux of each SN around Si II λ6355 line in our $v_{\rm Si\,II}$ sample. All the $v_{\rm Si\,II}$ measurements can be found in Table B1.

2.3.1 *Evaluation of host-galaxy contamination*

High-z SNe are often blended with their host galaxies. As mentioned in Section 2.1, we chose the background regions as carefully as possible to subtract the host-galaxy light when processing the spectrum. However, it is sometimes inevitable that the final spectrum could still suffer non-negligible contamination from their host galaxies. Here, we evaluate the effect of host-galaxy contamination on the $v_{\rm Si\,II}$ measurement.

Our method is based on Howell et al. (2005), using a χ^2 fitting technique to estimate the fraction of host-galaxy contamination in the SN spectrum. Howell et al. (2005) fit each SN spectrum with a library of SN templates of all types and a range of phases. The reddening, redshift (if not determined from the host galaxy), and fraction of host-galaxy contamination are derived by minimizing the difference between the observed SN spectrum and template spectrum. Instead of fitting the observed spectrum with templates of a wide range of parameter space (which could result in substantial degeneracy), we allow only specific SN and host-galaxy templates in the fitting. For the SN template, we use the `kaepora` data base (Siebert et al. 2019) to produce a mean spectrum given the exact phase and LC width (e.g. from Scolnic et al. 2018) of each SN in our sample. For the host-galaxy template, we first measure the host-galaxy photometry from the PS1 template images in *grizy* filters. We measure the photometry by placing an aperture of 1.5 arcsec radius at the SN location. This allows us to better constrain the host-galaxy spectral energy distribution (SED) near the SN birthplace. The measured photometry will then be used as input for the photometric redshift code Z–PEG to derive the best-fitting galaxy template and properties. Z–PEG fits the observed galaxy colours with galaxy SED templates

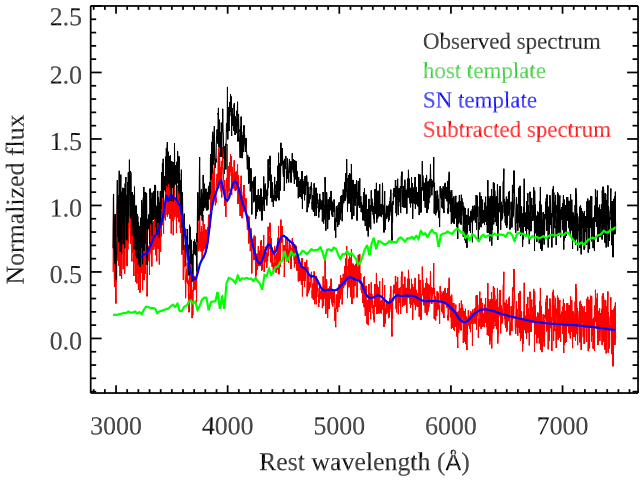

Figure 2. Result of host-galaxy subtraction for SN Ia PS1-190260. The black and red spectra represent the original SN spectrum and that after the host-galaxy subtraction, respectively. The green spectrum is the host-galaxy template determined from the host-galaxy photometry. The SN template produced by `kaepora` is shown in blue.

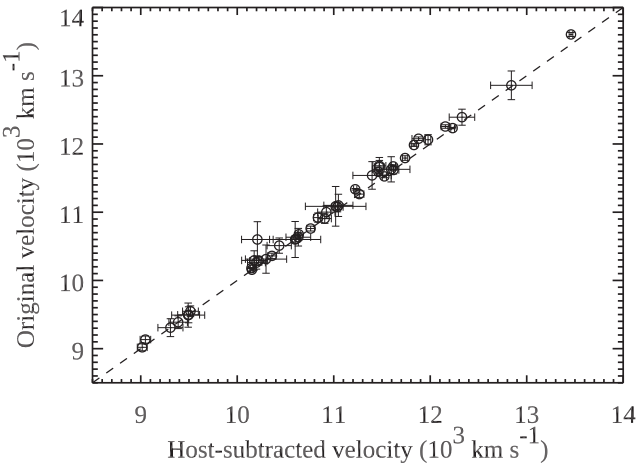

Figure 3. The Si II λ6355 velocity measured from the SN spectra before and after the host-galaxy template subtraction. The line of equality is shown in a dashed line.

corresponding to nine spectral types (SB, Im, Sd, Sc, Sbc, Sb, Sa, S0, and E). Here, we assume a Salpeter (1955) initial mass function (IMF). The photometry is corrected for the foreground Milky Way reddening with $R_V = 3.1$ and a (Cardelli, Clayton & Mathis 1989; CCM) reddening law. The details of the fitting procedure can be found in Pan et al. (2014).

Fig. 2 shows the result of host-galaxy subtraction from one of our SNe. Overall, the host-galaxy contamination of our sample is not significant. We determine a median fraction of host-galaxy contamination of only 17 per cent, with 45 out of 48 SNe having fractions lower than 50 per cent. The $v_{\rm Si\,II}$ comparison between the spectra before and after the host-galaxy template subtraction can be found in Fig. 3. The two measurements are consistent with each other, with a mean offset of 65 km s^{-1} and rms scatter of 101 km s^{-1}. Given that the difference in velocity is statistically insignificant, and not all the SNe in our sample have host-subtracted spectra available, we simply adopt the original velocity measurements for further analysis.

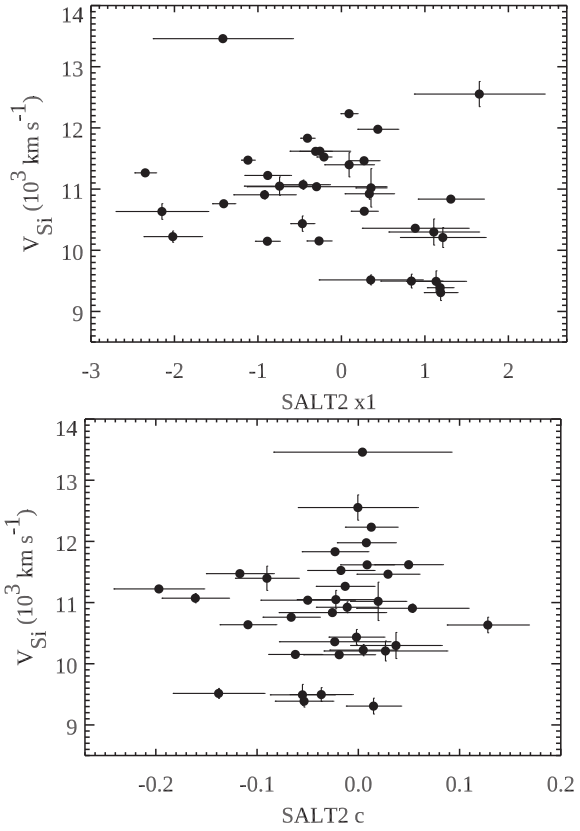

Figure 4. The Si II λ6355 velocity ($v_{\rm Si\,II}$) as a function of SN stretch x_1 (upper panel) and colour c (lower panel) derived by the SALT2 LC fitter (Guy et al. 2007).

3 RESULTS

In this section, we investigate the relationship between $v_{\rm Si\,II}$ and several critical parameters. Various methods are used when evaluating the trend of our data set, such as linear fitting with LINMIX (Kelly 2007) and weighted mean while comparing the difference between subgroups, if not mentioned otherwise.

3.1 Silicon velocity and light-curve parameters

We first compare the $v_{\rm Si\,II}$ with the SN photometric parameters. The SALT2 (Guy et al. 2007) stretch x_1 and colour c parameters measured in Scolnic et al. (2018) are used in the analysis. The x_1 parameter measures the LC width of SN Ia, a key parameter to calibrate the SN luminosities. Brighter SNe Ia tend to have LCs with slower decline rates or higher stretches (Phillips 1993). The colour parameter c measures the SN $(B-V)$ colour at maximum light, serving as another parameter in SN Ia standardization (e.g. Riess, Press & Kirshner 1996). Our $v_{\rm Si\,II}$ sample includes 35 SNe with x_1 and c measurements, of which only 3 are HV SNe Ia.

The $v_{\rm Si\,II}$ as a function of x_1 can be found in the upper panel of Fig. 4. We do not see a significant trend between $v_{\rm Si\,II}$ and x_1. No trend is found when comparing the HV and NV subgroups either. The results from PS1-MDS sample are generally consistent with low-z studies (e.g. Wang et al. 2009; Maguire et al. 2014; Dettman et al. 2021), although we note that the HV subgroup contains only three SNe in this analysis.

The $v_{\rm Si\,II}$ as a function of c can be found in the lower panel of Fig. 4. We do not detect any significant trend between $v_{\rm Si\,II}$ and the colour parameter c. Some previous studies showed that the HV SNe Ia tend to be redder than their NV counterparts (e.g. Wang et al. 2009; Foley et al. 2011). We note that the HV subgroup in our sample has a mean c 0.03 mag redder than the NV subgroup (at 3.5σ significance). However, we cannot conclusively claim the trend due to the small size of the HV subgroup (which contains only three HV SNe Ia in the analysis).

3.2 Silicon velocity and host-galaxy properties

The relation between $v_{\rm Si\,II}$ and host-galaxy properties at low-redshift was investigated by several recent studies (e.g. Wang et al. 2013; Pan et al. 2015; Pan 2020). For instance, Pan (2020) found a significant trend between $v_{\rm Si\,II}$ and host-galaxy stellar mass ($M_{\rm stellar}$) with SNe Ia discovered at $z < 0.2$, in the sense that HV SNe Ia tend to explode in massive galaxies, while NV SNe Ia can be found in either low-mass or massive galaxies. This trend was further confirmed by Dettman et al. (2021) with a different low-z data set.

We revisit this relationship with the PS1-MDS sample. The host-galaxy $M_{\rm stellar}$ studied in this work is determined by Z–PEG (see Section 2.3.1 for details). In contrast to Section 2.3.1, an elliptical aperture is used here to enclose the whole galaxy for measuring the global properties. Both $v_{\rm Si\,II}$ and host-galaxy stellar mass are measured consistently with those in Pan (2020). Our $v_{\rm Si\,II}$ sample includes 41 SNe with host-galaxy measurements, of which only 4 are HV SNe Ia. The result is shown in Fig. 5. While the trend between $v_{\rm Si\,II}$ and host-galaxy $M_{\rm stellar}$ is not statistically significant for the PS1-MDS sample alone, it generally shows good consistency with the low-z sample. Despite the small sample size, all the HV SNe Ia from PS1-MDS have host-galaxy $\log(M_{\rm stellar}) > 9.5\,{\rm M}_\odot$, while the NV SNe Ia can be found in galaxies with very low stellar mass (e.g. $M_{\rm stellar} \sim 10^6\,{\rm M}_\odot$). The difference in mean $\log(M_{\rm stellar})$ between HV and NV subgroups (considering both the low-z and PS1-MDS SNe) is $0.31 \pm 0.08\,{\rm M}_\odot$ (at 3.9σ significance), with HV subgroup having (on average) more massive host galaxies than that from NV subgroup.

We further examine the relationship between $v_{\rm Si\,II}$ and other host-galaxy properties, including the star formation rate (SFR) and specific SFR. Our analysis of the PS1-MDS sample does not reveal any significant trends, which is consistent with findings from previous low-z studies (e.g. Pan 2020). No significant trend is identified either when combining both the PS1-MDS and low-z data sets.

3.3 Silicon velocity and redshift

We next investigate the relationship between $v_{\rm Si\,II}$ and redshift. Foley (2012) compared the $v_{\rm Si\,II}$ distributions between low-z and high-z samples but found no significant difference between the two groups. We further explore this with our PS1-MDS sample. As shown in the left panel of Fig. 6, we do not see a significant trend between $v_{\rm Si\,II}$ and redshift when considering only the PS1-MDS sample. Fitting a straight line using the LINMIX gives a 73 per cent probability the slope is negative. In addition, no discrepancy is observed in terms of the mean redshift when separating the PS1-MDS sample into NV and HV subgroups. The difference in mean redshift calculated via bootstrap re-sampling between HV and NV subgroups is 0.03 ± 0.05 (at $< 1\sigma$ significance). However, we note that the mean value of the HV subgroup could be uncertain due to the small sample size of the PS1-only sample.

To further constrain the trend, we add the spectroscopic compilation studied in Foley (2012) to increase the number of high-z SNe. This compilation comprises the SNe discovered by both

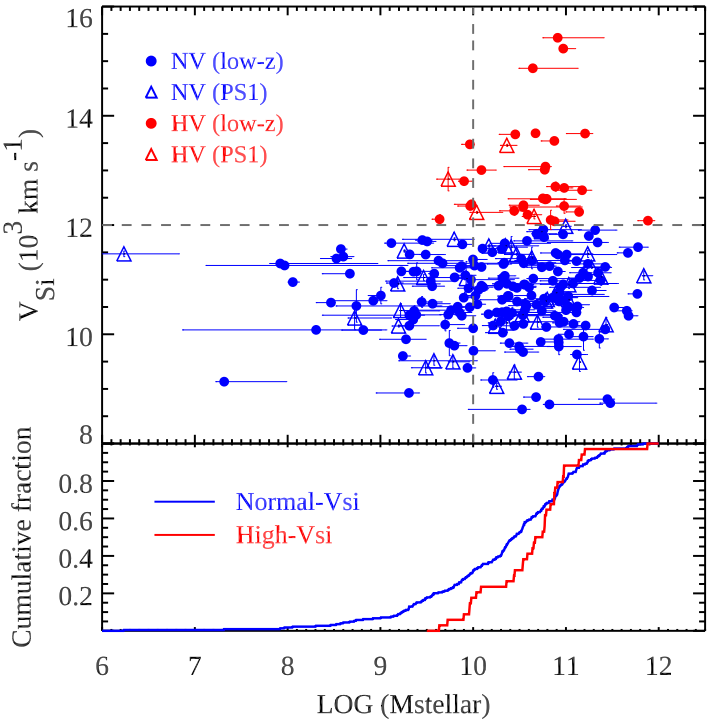

Figure 5. The Si II λ6355 velocities ($v_{\rm Si\,II}$) as a function of host-galaxy stellar mass ($M_{\rm stellar}$). The PS1-MDS SNe (this work) are represented by open triangles, and the low-z SNe from Pan (2020) are in solid circles. The HV and NV SNe Ia in each sample are shown in red and blue, respectively. The horizontal dashed line represents the criteria for splitting the sample in velocity space. The vertical dashed line represents the host-galaxy stellar mass of $\log(M_{\rm stellar}) = 10\,{\rm M}_{\odot}$. The bottom histograms show the cumulative fractions of $M_{\rm stellar}$ for HV (in red) and NV (in blue) SNe Ia.

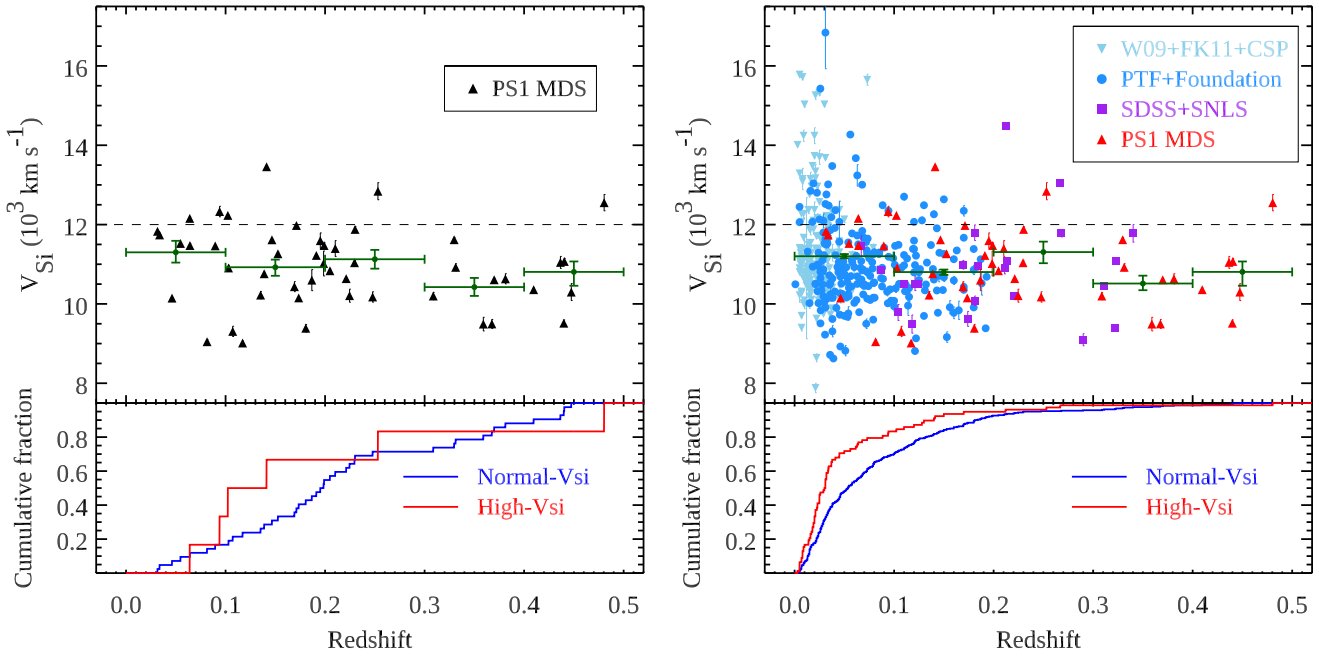

Figure 6. *Left:* The Si II λ6355 velocities ($v_{\rm Si\,II}$) as a function of redshift for PS1-MDS sample. The PS1-MDS sample (this work) is shown in black triangles. The mean $v_{\rm Si\,II}$ in bins of redshift is shown in green. The bottom histograms show the cumulative fractions of redshift for HV (in red) and NV (in blue) SNe Ia. *Right:* The same as the left panel, but combining the SNe Ia found in PS1-MDS (in red triangles), SDSS/SNLS (in purple squares), PTF/Foundation (in blue circles), and W09/FK11/CSP (in blue triangles).

Sloan Digital Sky Survey-II (SDSS-II) Supernovae Survey (Frieman et al. 2008) and Supernova Legacy Survey (SNLS; Astier et al. 2006) programmes. We re-measured the $v_{\rm Si\,II}$ for these SNe with the consistent method as that described in Section 2.3. The same phase cut (see Section 2.2) is adopted to these SNe to obtain the near-peak measurements. A total of 23 high-z SNe are added to our sample and listed in Table B1. To include the low-z sample, we use the spectroscopic compilation studied in Pan et al. (2015) and

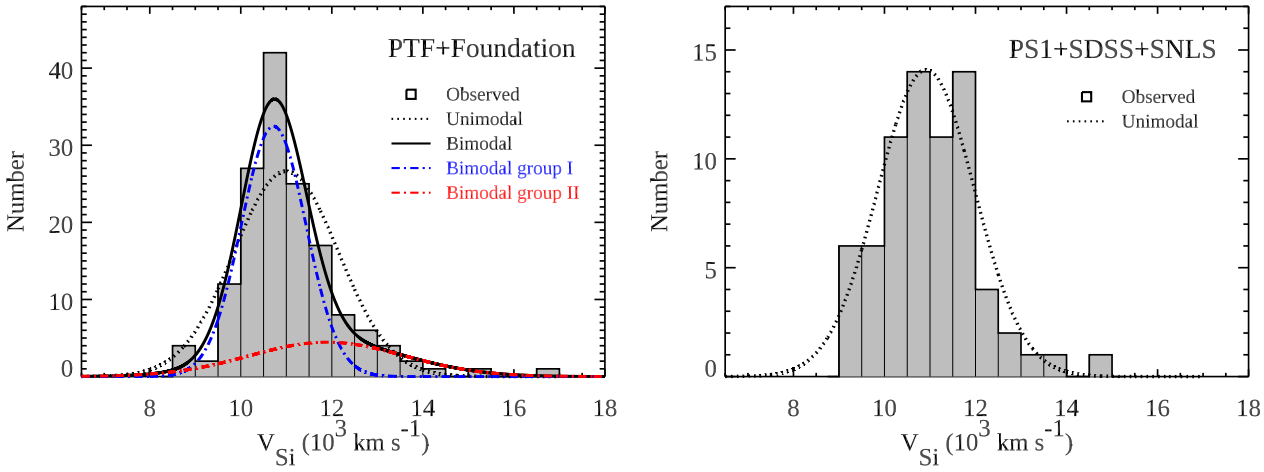

Figure 7. *Left*: The histogram shows the Si II λ6355 velocity ($v_{\rm Si\,II}$) distribution from the low-z PTF (Pan 2020) and Foundation (Dettman et al. 2021) SNe Ia. The black dotted and solid curves represent the unimodal and bimodal fits from the maximum-likelihood method (Zhang et al. 2020), respectively. The blue and red dash–dotted curves represent the two components in the bimodal fit. *Right*: The same as the left panel, but with the high-z PS1-MDS SNe (this work) and SDSS/SNLS SNe from Foley (2012). Here, only the unimodal distribution can provide a reasonable fit to the high-z data set.

Dettman et al. (2021). The SNe studied in Pan et al. (2015) were all discovered by the Palomar Transient Factory (PTF; Law et al. 2009). The Dettman et al. (2021) sample comprises low-z SNe Ia from the Carnegie Supernova Project (CSP; Hamuy et al. 2006), Wang et al. (2009, hereafter W09), Foley & Kasen (2011, hereafter FK11), and Foundation Supernova Survey (Foley et al. 2018). The $v_{\rm Si\,II}$ of these low-z SNe were measured consistently. These low-z samples contain 388 SNe Ia with near-peak $v_{\rm Si\,II}$ measurements.

The result is shown in the right panel of Fig. 6. With such a large compilation, we still find no significant trend between $v_{\rm Si\,II}$ and redshift up to $z \sim 0.5$. LINMIX gives only a 68 per cent probability the slope is negative when fitting a straight line to the whole sample. However, it is worth noting that the mean $v_{\rm Si\,II}$ of SNe in the $z < 0.1$ bin is significantly higher than that for the $0.1 < z < 0.5$ bin (at 4.4σ significance). When separating our sample into HV and NV subgroups, we also find some evidence that the HV SNe Ia are more likely to explode in the low-z Universe than their NV counterparts. The difference in mean redshift between HV and NV subgroups is 0.027 ± 0.007 (at 3.9σ significance), with the HV subgroup having (on average) lower redshift than the NV subgroup. A Kolmogorov–Smirnov (K–S) test gives a p value of 8×10^{-5}, rejecting the null hypothesis that the NV and HV SNe Ia have the same redshift distributions.

Since no obvious trend is identified between $v_{\rm Si\,II}$ and redshift for the PS1-only sample (or even a larger sample combining all the high-z SNe from PS1, SDSS, and SNLS), we suspect that the trend between HV and NV SNe Ia found above could be due to the inclusion of low-z samples. While the smaller sample size of our high-z sample may play a role, the different selections and strategies between low-z and high-z surveys could complicate our interpretation and thus need careful consideration. A detailed discussion on this can be found in Section 4.2.

4 DISCUSSION

4.1 Silicon velocity distribution

Zhang et al. (2020) studied the $v_{\rm Si\,II}$ distribution with a large sample of low-z SNe Ia. They found that the $v_{\rm Si\,II}$ shows a significant bimodal Gaussian distribution, with one group having a mean $v_{\rm Si\,II} = 11000 \pm 700$ km s^{-1} and the other group having a mean $v_{\rm Si\,II} = 12300 \pm 1800$ km s^{-1}. Here, we designate the SNe in these two velocity distributions as group-I (with lower mean $v_{\rm Si\,II}$) and group-II (with higher mean $v_{\rm Si\,II}$) to distinguish them from the conventional NV and HV SNe Ia. Zhang et al. (2020) calculated a population fraction of 65 per cent and 35 per cent for group-I and group-II SNe, respectively. While it is unclear if these populations are physically distinct, a bimodal Gaussian distribution can adequately describe the $v_{\rm Si\,II}$ distribution of low-z SNe Ia.

However, the results from Zhang et al. (2020) could be strongly biased, as a substantial fraction of their sample were discovered from the galaxy-targeted surveys (from the `kaepora` data base; Siebert et al. 2019). Their result may not represent the intrinsic population ratio of group-II to group-I SNe, given that the HV SNe Ia (pre-dominantly in group-II) are preferentially discovered in massive galaxies. Here, we revisit their works with low-z untargeted samples, including SNe from PTF and Foundation surveys. To facilitate a better comparison with Zhang et al. (2020), we apply a redshift cut on these samples and use only SNe Ia at $z < 0.09$.

We repeat the same statistical technique (the maximum-likelihood method) as that performed in Zhang et al. (2020). This technique has the advantage that it is not sensitive to the bin size of the distribution during the fitting. The result is shown in the left panel of Fig. 7. We find a similar bimodal $v_{\rm Si\,II}$ distribution with our sample. A modified version of Akaike Information Criterion (AICc; Sugiura 1978) of 2580 and 2551 are calculated for unimodal fit and bimodal fit of our $v_{\rm Si\,II}$ distribution, respectively. This indicates that the bimodal distribution gives a significantly better (e.g. a difference larger than six; Mukherjee et al. 1998) fit than the unimodal fit. However, our low-z SNe tend to show quite different population fractions and mean velocities between the two groups from that of Zhang et al. (2020). We measure a mean $v_{\rm Si\,II} = 10700 \pm 700$ km s^{-1} and $v_{\rm Si\,II} = 11900 \pm 1700$ km s^{-1} and population fractions of 76 per cent and 24 per cent, for group-I and group-II SNe, respectively. Our sample has an averagely lower $v_{\rm Si\,II}$ (for both velocity groups), and a lower fraction of SNe in group-II than that of Zhang et al. (2020). We believe this should be closer to the intrinsic $v_{\rm Si\,II}$ distribution.

We next examine the $v_{\rm Si\,II}$ distribution for high-z SNe Ia. The high-z sample studied here is the same as that studied in Section 3.3 (from the PS1-MDS, SDSS, and SNLS). The result is shown in the right panel of Fig. 7. In contrast to the low-z sample, we find the bimodal

distribution fails to provide a reasonable fit to our high-z sample (we therefore only present the unimodal fit in the figure). An AICc of 1198 and 1199 is calculated for unimodal fit and bimodal fit, respectively. This indicates that the bimodal distribution is not favoured over the unimodal distribution. A mean $v_{\rm Si\,II} = 10900 \pm 1100$ km s^{-1} is determined from the unimodal fit.

It is unclear if the difference in $v_{\rm Si\,II}$ distributions between the low-z and high-z samples is due to the relatively small size of the current high-z sample. It is also worth noting that the conventional criterion to separate the HV and NV SNe Ia (i.e. $v_{\rm Si\,II} \sim 12000$ km s^{-1}) cannot separate the two velocity groups unambiguously. There is a substantial overlap in the velocity space between group-I and group-II SNe. From the bimodal fit of our low-z sample, there is 3.5 per cent of SNe in group-I that are classified as HV SN Ia and 52.5 per cent of SNe in group-II that are classified as NV SNe Ia. Studies on each individual group of SNe using this velocity criterion would unavoidably suffer some contamination from the other group. Including additional parameters (such as carbon and nebular spectral features) could be helpful in breaking the degeneracy in velocity space.

The large dispersion of $v_{\rm Si\,II}$ found in group-II SNe could be linked to the detonations of sub-Chandrasekhar-mass white dwarfs (WDs) based on a few theoretical studies. Polin et al. (2019) studied the 1D sub-Chandrasekhar-mass WD explosion models and found they can produce a wide range of $v_{\rm Si\,II}$, including both HV and NV SNe Ia. Their results showed that the relation between SN Ia luminosity and $v_{\rm Si\,II}$ could be well explained by two populations, with one associated with the Chandrasekhar-mass WD explosions and the other with the sub-Chandrasekhar-mass WD explosions. In contrast, Shen et al. (2021) used multidimensional radiation transport calculations and produced the bulk of observed SNe Ia from simply the double detonations of sub-Chandrasekhar-mass WDs. However, it is unclear if this scenario alone can explain the bimodal $v_{\rm Si\,II}$ distribution found for low-z SNe Ia. A large sample with well-measured ejecta velocities would be critical to better constrain the models.

4.2 The redshift distributions of HV and NV SNe Ia

In Section 3.3, we investigate the relation between $v_{\rm Si\,II}$ and redshift but find no significant trend with either the PS1-only sample or a large spectroscopic compilation. However, we find the HV SNe Ia tend to show a notable difference in redshift distribution compared to NV SNe Ia, in the sense that the HV SNe Ia are more prevalent at low-z. Since this trend vanishes when considering solely the high-z samples, we suspect that the discrepancy between the low-z and high-z surveys (such as selection effects) could be the underlying factor driving the trend.

First, the Malmquist bias may have some impact if the HV SNe Ia are systematically fainter than the NV SNe Ia. Under such circumstances, we would expect that the HV SNe Ia will be more difficult to find at high-z. However, existing evidence suggested that the brightness of HV and NV SNe Ia are generally comparable (e.g. Wang et al. 2009, 2013). This is also supported by the lack of trend in the relation between $v_{\rm Si\,II}$ and LC width as noted by many previous studies (e.g. Wang et al. 2009; Maguire et al. 2014; Dettman et al. 2021). These findings make the Malmquist bias less likely to be the underlying source that drives the preference of HV SNe Ia to be discovered at low-z surveys. However, there is likely a colour difference between NV and HV SNe Ia reported by previous studies. None the less, we would argue the colour difference should not be significant enough (< 0.1 mag on average; Foley & Kasen 2011, see also the lower panel of Fig. 4) to influence the decision we made to select the Ia-like objects. Moreover, if HV and NV SNe Ia indeed differ in brightness and colour, we should also anticipate a trend from our high-z samples, given their broad redshift coverage (i.e. from $z \sim 0.1 - 0.5$), as opposed to a trend caused solely by samples at $z \lesssim 0.1$. A larger high-z sample will be critical for further investigation.

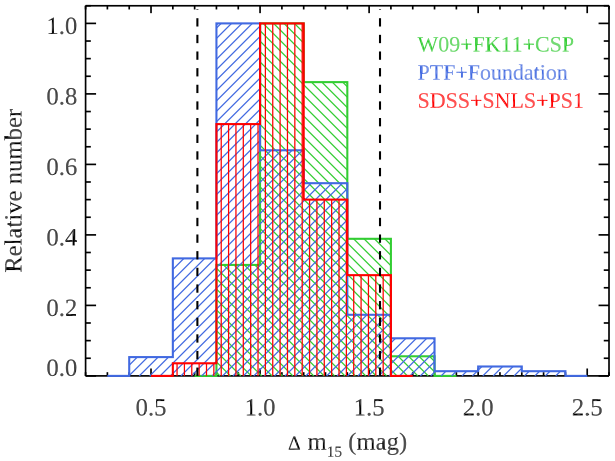

Figure 8. The Δm_{15} distributions of different subsamples (grouped in terms of their redshifts). The vertical dashed lines represent the minimum and maximum Δm_{15} that the HV SNe Ia have in this work.

We next explore the potential impact of different Δm_{15} (defined as B band decline 15 d after peak B-band brightness) distributions between low-z and high-z surveys. Fig. 8 shows the Δm_{15} distributions of various subsamples in this work. The Δm_{15} is converted from the light-curve stretch parameters (e.g. Guy et al. 2007; Conley et al. 2008) measured by previous studies. It is clear that the Δm_{15} distributions of different subsamples generally cover the Δm_{15} range of HV SNe Ia investigated in this work ($0.71 < \Delta m_{15} < 1.55$ mag, as denoted by the dashed lines in Fig. 8). However, differences between subsamples are evident. Notably, the low-z samples (such as PTF and Foundation) exhibit an excess of high-Δm_{15} SNe (e.g. $\Delta m_{15} \gtrsim 1.5$ mag) compared to the high-z samples. To assess if the difference in Δm_{15} distributions could impact our results, we construct a new subsample by restricting the decline rates of our SNe to $0.7 < \Delta m_{15} < 1.6$ mag (i.e. consistent with the minimum and maximum Δm_{15} of our HV SN Ia sample). Even with this Δm_{15}-restricted sample, the difference in redshift distributions between HV and NV SNe Ia remains significant. A K–S test gives a p-value of 9×10^{-4}, rejecting the null hypothesis that the NV and HV SNe Ia have the same redshift distributions.

Another potential source of disparity between low-z and high-z surveys could stem from the selection of distinct host-galaxy environments, as HV and NV SNe Ia tend to reside in galaxies with different $M_{\rm stellar}$ (as discussed in Section 3.2). Fig. 9 compares the distributions of host-galaxy $M_{\rm stellar}$ among various subsamples. The comparison is made only for those SNe with $v_{\rm Si\,II}$ measurements available. It is notable that the W09/FK11/CSP samples exhibit a strong bias towards massive galaxies. A K–S test gives a p-value of 4×10^{-4}, rejecting the null hypothesis that the PS1-MDS and W09/FK11/CSP samples have the same host-galaxy $M_{\rm stellar}$ distributions. This is probably not surprising given that the W09/FK11/CSP samples are mainly galaxy-targeted. In contrast, the $M_{\rm stellar}$ distributions of PTF, Foundation, and PS1-MDS samples are similar to each other (based on the p-value of the K–S test). After excluding the W09/FK11/CSP samples from the analysis, the difference in mean redshift between

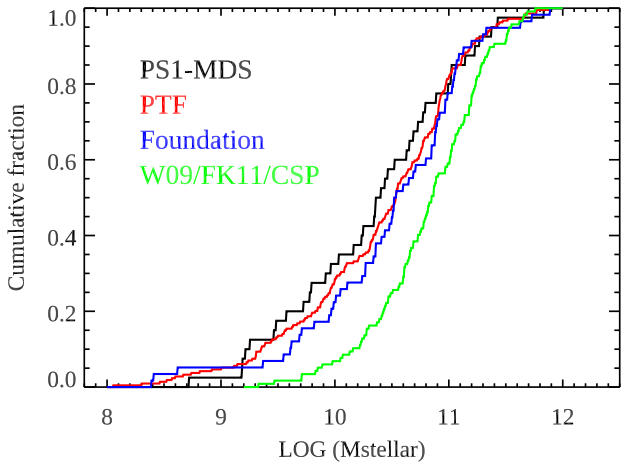

Figure 9. Cumulative fractions of host-galaxy stellar mass ($M_{\rm stellar}$) for various samples: PS1-MDS (in black), PTF (in red), Foundation (in blue), and W09/FK11/CSP (in green) samples. Only those SNe Ia with $v_{\rm Si\,II}$ measurements available are included in the figure.

HV and NV subgroups becomes 0.02 ± 0.01 (at 2σ significance), and the K–S test gives a p-value of 0.02, still rejecting the null hypothesis that the NV and HV SNe Ia have the same redshift distributions. While it is evident that excluding the SNe from galaxy-targeted surveys greatly reduces the significance of the redshift difference between HV and NV SNe Ia, it does not eliminate the entire trend. This probably implies the difference in host-galaxy $M_{\rm stellar}$ may not be the only factor contributing to the disparity between low-z and high-z surveys. However, it is still expected to affect the relative fractions between HV and NV SNe Ia as a function of redshift, as previous observations have shown that the galaxy $M_{\rm stellar}$ functions tend to evolve over time, with galaxies at higher redshift containing on average less $M_{\rm stellar}$ (e.g. Davidzon et al. 2017). This trend was also identified with host galaxies of SNe Ia (Sullivan et al. 2010).

While PTF and Foundation samples may have additional complicated selections compared to PS1-MDS, we would argue whether they have a substantial impact on our results, given the similarities of HV and NV SNe Ia (both photometrically and spectroscopically). In fact, we find that the difference in redshift distributions between HV and NV SNe Ia persists even when considering solely the PTF and Foundation samples or just the PTF sample. This is against the argument that the discrepancy between low-z and high-z surveys is the main cause of the trend. If this difference is linked to the progenitor properties of SNe Ia, it may suggest that HV SNe Ia (and a subset of NV SNe Ia) tend to have a much longer delay time (i.e. the time between the progenitor star formation and the subsequent SN Ia explosion) and only becomes significantly prevalent at low-z Universe. To fully understand and disentangle various effects, a larger high-z sample with ejecta velocity measurements will be essential in the future.

4.3 Implications on SN Ia cosmology

Using a new SN Ia colour model, Brout & Scolnic (2021) suggested that the SN Ia intrinsic scatter is likely dominated by the R_V variation of the dust around SN. They found the SNe Ia in massive galaxies have on average lower R_V than those in low-mass galaxies, and this difference can explain the trend between Hubble residuals and host-galaxy $M_{\rm stellar}$ (e.g. Sullivan et al. 2010). They also showed that the SN Ia colour distribution is inconsistent with a symmetric Gaussian distribution, with an excess of red SNe compared with the blue SNe. These red SNe were found to present a larger scatter of distance modulus residuals than the blue SNe.

While Brout & Scolnic (2021) proposed that the host-galaxy correlation with SN Ia luminosity is due to the variation in dust properties rather than the luminosities of different progenitor systems, it is not clear yet whether this dust variation is intrinsic to the host galaxies (e.g. from the interstellar medium) or the SN progenitor systems. Different SN Ia explosion scenarios could result in very different dust properties at the SN location. For instance, theoretical studies suggested that the double detonations of sub-Chandrasekhar-mass WDs are likely to have intrinsically different dust properties from that of Chandrasekhar-mass WD explosions (e.g. Polin et al. 2019; Shen et al. 2021). They tend to be redder due to the line blanketing originating from the ashes of the helium shell (although this may also depend on the viewing angle in the model).

Observationally, Wang et al. (2009) suggested that the HV SN Ia prefers a reddening law of lower R_V than that of NV SN Ia. Assuming most (if not all) of the SNe Ia in the group-II of bimodal $v_{\rm Si\,II}$ distribution share the same dust properties as that of HV SNe Ia, this may qualitatively explain the findings in Brout & Scolnic (2021), given their preference for lower R_V and massive host galaxies. While the group-II SNe represent only 24 per cent of the total SNe Ia in our low-z sample (see Section 4.1), this fraction will be raised to ∼40 per cent if we only consider the SNe in galaxies of $\log(M_{\rm stellar}) > 10\,{\rm M}_{\odot}$. On the other hand, Salim, Boquien & Lee (2018) found that the galaxy dust properties tend to vary with the stellar mass, with massive and quiescent galaxies having lower R_V than that of star-forming galaxies. While HV SN Ia host galaxies are generally massive, Pan et al. (2015) found that more than half of the HV SN Ia host galaxies are not quiescent galaxies. Therefore, the dust from the interstellar medium alone seems challenging to explain the preference of HV SNe Ia for having a reddening law of lower R_V. The nature of the progenitor system could also contribute to the creation of these unique dust properties. If the group-II SNe are associated with the sub-Chandrasekhar-mass explosions, they could be a significant source of distance uncertainties. This is also evident from the previous studies that showed SNe Ia in low-mass galaxies are better standard candles than those in massive galaxies (e.g. Kim, Kang & Lee 2019).

By examining the deviations from a zero-colour SN Ia that is corrected for host-galaxy reddening, Foley et al. (2011) determined the intrinsic $B - V$ colour (at peak luminosity) for a sample of SNe Ia. They found the $v_{\rm Si\,II}$ is correlated with the SN intrinsic colour, with higher velocity SNe being intrinsically redder than the lower velocity counterparts (the so-called velocity–colour relation). We look into this relation by examining the SN intrinsic colour as a function of redshift. We first construct a cosmological sample by including the SNe from our full compilation (i.e. those shown in the right panel of Fig. 6) that have Hubble residuals (HRs; defined as the difference between the observed peak SN apparent magnitude and that expected in the assumed cosmological model) measured in Scolnic et al. (2018) and Dettman et al. (2021). The HRs were measured consistently in both studies. We then compare this sample with the 'all' sample, which includes both the cosmological sample and all other SNe that do not meet the cosmological criteria. The SN intrinsic colour is converted directly from the $v_{\rm Si\,II}$ with the velocity–colour relation studied in Foley et al. (2011). As shown in Fig. 10, it is evident that the mean intrinsic colour of SNe Ia is redder for the low-z sample, with the SNe at $z < 0.1$ being 0.015 mag redder than those at $z > 0.1$ (at 4.3σ significance). However, the trend vanishes ($< 2\sigma$) if we only consider the SNe in the cosmological sample. This implies

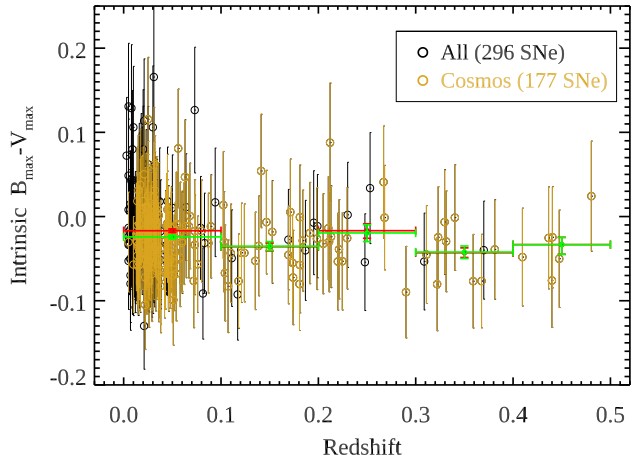

Figure 10. The black open circles show the SN Ia intrinsic colour (as converted from the Si II λ6355 velocity) as a function of redshift, where the golden open circles represent the SNe only in the cosmological sample. The mean intrinsic colour in bins of redshift is shown in red and green solid circles for the original and cosmological samples, respectively.

that the difference in intrinsic colour (as converted from velocity) between low-z and high-z samples can be effectively removed by the conventional cosmological cuts.

We next investigate the potential distance bias in cosmology by examining the relation between HR and $v_{\rm Si\,II}$. Siebert et al. (2020) found a possible trend (in 2.7σ) between $v_{\rm Si\,II}$ and HR, in the sense that higher velocity SNe Ia tend to show negative average HRs, while lower velocity SNe Ia tend to show positive average HRs. However, this trend becomes insignificant if using the SNe mainly discovered by untargeted surveys (Dettman et al. 2021). The HR as a function of $v_{\rm Si\,II}$ and SN intrinsic colour with our sample are shown in Fig. 11. This is the same cosmological sample as that shown in Fig. 10. We find that the HV and redder (i.e. with positive intrinsic colour) SNe tend to show negative average HRs, while their counterparts tend to show positive average HRs. Although our results are generally consistent with the previous studies, the trends are not statistically significant, with differences of 0.044 ± 0.023 mag (1.9σ) and 0.038 ± 0.021 mag (1.8σ) between the subgroups in HR–$v_{\rm Si\,II}$ and HR–colour relations, respectively. Nevertheless, we note that the current number of HV SNe Ia in our cosmological sample is considerably smaller than that of NV SNe Ia.

5 CONCLUSIONS

In this paper, we measure the Si II λ6355 velocity ($v_{\rm Si\,II}$) from SNe Ia discovered by the PS1-MDS and investigate the relations between $v_{\rm Si\,II}$ and other parameters, including LC width, colour, and host galaxy properties. Our main findings are:

(i) We do not see significant trends between $v_{\rm Si\,II}$ and either LC width x_1 or colour c. For the relation with host-galaxy $M_{\rm stellar}$, it is difficult to claim the trend with the PS1-MDS sample alone, given its small sample size. However, we note that the trend stays significant after combining our PS1-MDS SNe with those from low-z studies, in the sense that HV SNe Ia are more likely to be found in massive galaxies.

(ii) No significant trends are identified between $v_{\rm Si\,II}$ and redshift using either the PS1-only sample or a large spectroscopic compilation that includes additional low-z and high-z data sets. However, with the large sample, we find a significant probability that HV and NV SNe Ia may have distinct redshift distributions, with HV SNe Ia being more prevalent in the local Universe. Different selections between low-z and high-z surveys could play a role. Nevertheless, we do not rule out the possibility that the progenitors of HV SNe Ia (and perhaps a subset of NV SNe Ia) may favour explosion scenarios of long delay times.

(iii) We confirm the previous findings that the $v_{\rm Si\,II}$ distribution of low-z SNe Ia shows a significant bimodal distribution. The two groups substantially overlap in the velocity space, with a fraction of 76 per cent and 24 per cent for SNe in group-I and group-II, respectively. However, this bimodality becomes insignificant for the high-z sample studied in this work.

(iv) Our results are also in line with recent cosmological studies, which have shown that SNe Ia in massive galaxies typically exhibit lower R_V than those in low-mass galaxies. This could possibly be explained by assuming that a large fraction of SNe Ia in massive galaxies share similar dust properties with HV SNe Ia.

(v) By converting the $v_{\rm Si\,II}$ to the SN intrinsic colour, we show that the mean intrinsic colour of SNe Ia appears to be redder in

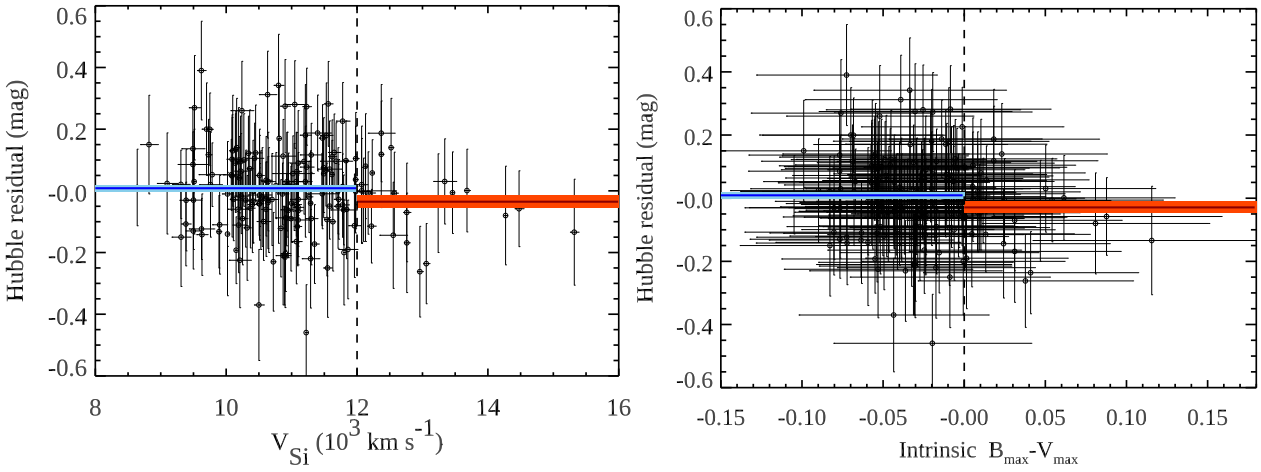

Figure 11. *Left*: The Hubble residuals as a function of Si II λ6355 velocity ($v_{\rm Si\,II}$). The vertical dashed line represents the criterion used to separate the velocity bins. The solid lines in blue and red represent the weighted mean of the residuals in bins of velocity, and the shaded regions show the 1σ uncertainty of the weighted mean. *Right*: The same as the left panel, but with SN Ia intrinsic colour converted from the $v_{\rm Si\,II}$ using the velocity–colour relation (Foley, Sanders & Kirshner 2011).

the local Universe. However, this trend vanishes when considering only the SNe in the cosmological sample. Furthermore, we confirm that the HV SNe Ia tend to have negative average HRs than their counterparts, but the trend is not statistically significant with our sample.

Future studies with precise spectroscopic measurements spanning a wide range of redshift would be crucial to differentiate between SN Ia explosion scenarios and investigate their potential evolution or change in demographics. Such investigations will enormously improve our understanding of the nature of SNe Ia and refine their utility in cosmological studies.

ACKNOWLEDGEMENTS

This work was supported by the National Science and Technology Council (NSTC grant 109-2112-M-008-031-MY3).

DATA AVAILABILITY

The SN Ia spectra from PS1-MDS will be made available in the WISeREP archive (Yaron & Gal-Yam 2012). Other data underlying this article will be shared on reasonable request to the corresponding author.

REFERENCES

Abbott T. M. C. et al., 2019, ApJ, 872, L30
Aldering G. S., Supernova Factory N., 2007, BAAS, 39, 191
Astier P. et al., 2006, A&A, 447, 31
Balland C. et al., 2009, A&A, 507, 85
Balland C. et al., 2018, A&A, 614, A134
Blondin S., Tonry J. L., 2007, ApJ, 666, 1024
Blondin S. et al., 2006, AJ, 131, 1648
Bronder T. J. et al., 2008, A&A, 477, 717
Brout D., Scolnic D., 2021, ApJ, 909, 26
Brout D. et al., 2022, ApJ, 938, 110
Cardelli J. A., Clayton G. C., Mathis J. S., 1989, ApJ, 345, 245
Cepa J. et al., 2003, in Iye M., Moorwood A. F. M., eds, Proc. SPIE Conf. Ser. Vol. 4841, Instrument Design and Performance for Optical/Infrared Ground-based Telescopes. SPIE, Bellingham, p.1739
Childress M. J., Filippenko A. V., Ganeshalingam M., Schmidt B. P., 2014, MNRAS, 437, 338
Conley A. et al., 2008, ApJ, 681, 482
Davidzon I. et al., 2017, A&A, 605, A70
Dettman K. G. et al., 2021, ApJ, 923, 267
Dressler A. et al., 2011, PASP, 123, 288
Faber S. M. et al., 2003, in Iye M., Moorwood A. F. M., eds, Proc. SPIE Conf. Ser. Vol. 4841, Instrument Design and Performance for Optical/Infrared Ground-based Telescopes. SPIE, Bellingham, p.1657
Fabricant D., Cheimets P., Caldwell N., Geary J., 1998, PASP, 110, 79
Fabricant D. et al., 2005, PASP, 117, 1411
Foley R. J., 2012, ApJ, 748, 127
Foley R. J., 2013, MNRAS, 435, 273
Foley R. J., Kasen D., 2011, ApJ, 729, 55 (FK11)
Foley R. J. et al., 2008, ApJ, 684, 68
Foley R. J., Sanders N. E., Kirshner R. P., 2011, ApJ, 742, 89
Foley R. J. et al., 2018, MNRAS, 475, 193
Frieman J. A. et al., 2008, AJ, 135, 338
Gerardy C. L. et al., 2004, ApJ, 607, 391
Guy J. et al., 2007, A&A, 466, 11
Hamuy M. et al., 2006, PASP, 118, 2
Hook I. M., Jørgensen I., Allington-Smith J. R., Davies R. L., Metcalfe N., Murowinski R. G., Crampton D., 2004, PASP, 116, 425
Howell D. A. et al., 2005, ApJ, 634, 1190
Howell D. A., Sullivan M., Conley A., Carlberg R., 2007, ApJ, 667, L37
Jones D. O. et al., 2019, ApJ, 881, 19
Jones D. O., Kenworthy W. D., Dai M., Foley R. J., Kessler R., Pierel J. D. R., Siebert M. R., 2022, ApJ, 951, 22
Kelly B. C., 2007, ApJ, 665, 1489
Kessler R. et al., 2009, ApJS, 185, 32
Kim Y.-L., Kang Y., Lee Y.-W., 2019, J. Korean Astron. Soc., 52, 181
Law N. M. et al., 2009, PASP, 121, 1395
Li W. et al., 2021, ApJ, 906, 99
Maeda K. et al., 2010, Nature, 466, 82
Maguire K. et al., 2014, MNRAS, 444, 3258
Maguire K. et al., 2018, MNRAS, 477, 3567
Marshall J. L. et al., 2008, in McLean I. S., Casali M. M., eds, Proc. SPIE Conf. Ser. Vol. 7014, Ground-based and Airborne Instrumentation for Astronomy II. SPIE, Bellingham, p.701454
Mazzali P. A. et al., 2005, ApJ, 623, L37
Miknaitis G. et al., 2007, ApJ, 666, 674
Mukherjee S., Feigelson E. D., Jogesh Babu G., Murtagh F., Fraley C., Raftery A., 1998, ApJ, 508, 314
Nicolas N. et al., 2021, A&A, 649, A74
Pakmor R. et al., 2022, MNRAS, 517, 5260
Pan Y.-C., 2020, ApJ, 895, L5
Pan Y.-C. et al., 2014, MNRAS, 438, 1391
Pan Y. C., Sullivan M., Maguire K., Gal-Yam A., Hook I. M., Howell D. A., Nugent P. E., Mazzali P. A., 2015, MNRAS, 446, 354
Perlmutter S. et al., 1999, ApJ, 517, 565
Phillips M. M., 1993, ApJ, 413, L105
Polin A., Nugent P., Kasen D., 2019, ApJ, 873, 84
Rest A. et al., 2014, ApJ, 795, 44
Riess A. G., Press W. H., Kirshner R. P., 1996, ApJ, 473, 88
Riess A. G. et al., 1998, AJ, 116, 1009
Riess A. G. et al., 2007, ApJ, 659, 98
Salim S., Boquien M., Lee J. C., 2018, ApJ, 859, 11
Salpeter E. E., 1955, ApJ, 121, 161
Schmidt G. D., Weymann R. J., Foltz C. B., 1989, PASP, 101, 713
Scolnic D. M. et al., 2018, ApJ, 859, 101
Shen K. J., Boos S. J., Townsley D. M., Kasen D., 2021, ApJ, 922, 68
Siebert M. R. et al., 2019, MNRAS, 486, 5785
Siebert M. R., Foley R. J., Jones D. O., Davis K. W., 2020, MNRAS, 493, 5713
Silverman J. M., Vinkó J., Marion G. H., Wheeler J. C., Barna B., Szalai T., Mulligan B. W., Filippenko A. V., 2015, MNRAS, 451, 1973
Sugiura N., 1978, Commun. Statist. Theory and Methods, 7, 13
Sullivan M., Ellis R. S., Howell D. A., Riess A., Nugent P. E., Gal-Yam A., 2009, ApJ, 693, L76
Sullivan M. et al., 2010, MNRAS, 406, 782
Sullivan M. et al., 2011, ApJ, 737, 102
Suzuki N. et al., 2012, ApJ, 746, 85
Walker E. S. et al., 2011, MNRAS, 410, 1262
Wang L. et al., 2003, ApJ, 591, 1110
Wang X. et al., 2009, ApJ, 699, L139 (W09)
Wang X., Wang L., Filippenko A. V., Zhang T., Zhao X., 2013, Science, 340, 170
Wang X., Chen J., Wang L., Hu M., Xi G., Yang Y., Zhao X., Li W., 2019, ApJ, 882, 120
Yaron O., Gal-Yam A., 2012, PASP, 124, 668
Zhang K. D. et al., 2020, MNRAS, 499, 5325

SUPPORTING INFORMATION

Supplementary data are available at *MNRAS* online.

suppl_data

Please note: Oxford University Press is not responsible for the content or functionality of any supporting materials supplied by the authors. Any queries (other than missing material) should be directed to the corresponding author for the article.

APPENDIX A: THE Si II λ6355 FEATURE OF THE PS1-MDS $v_{\rm Si\,II}$ SAMPLE IN THIS WORK

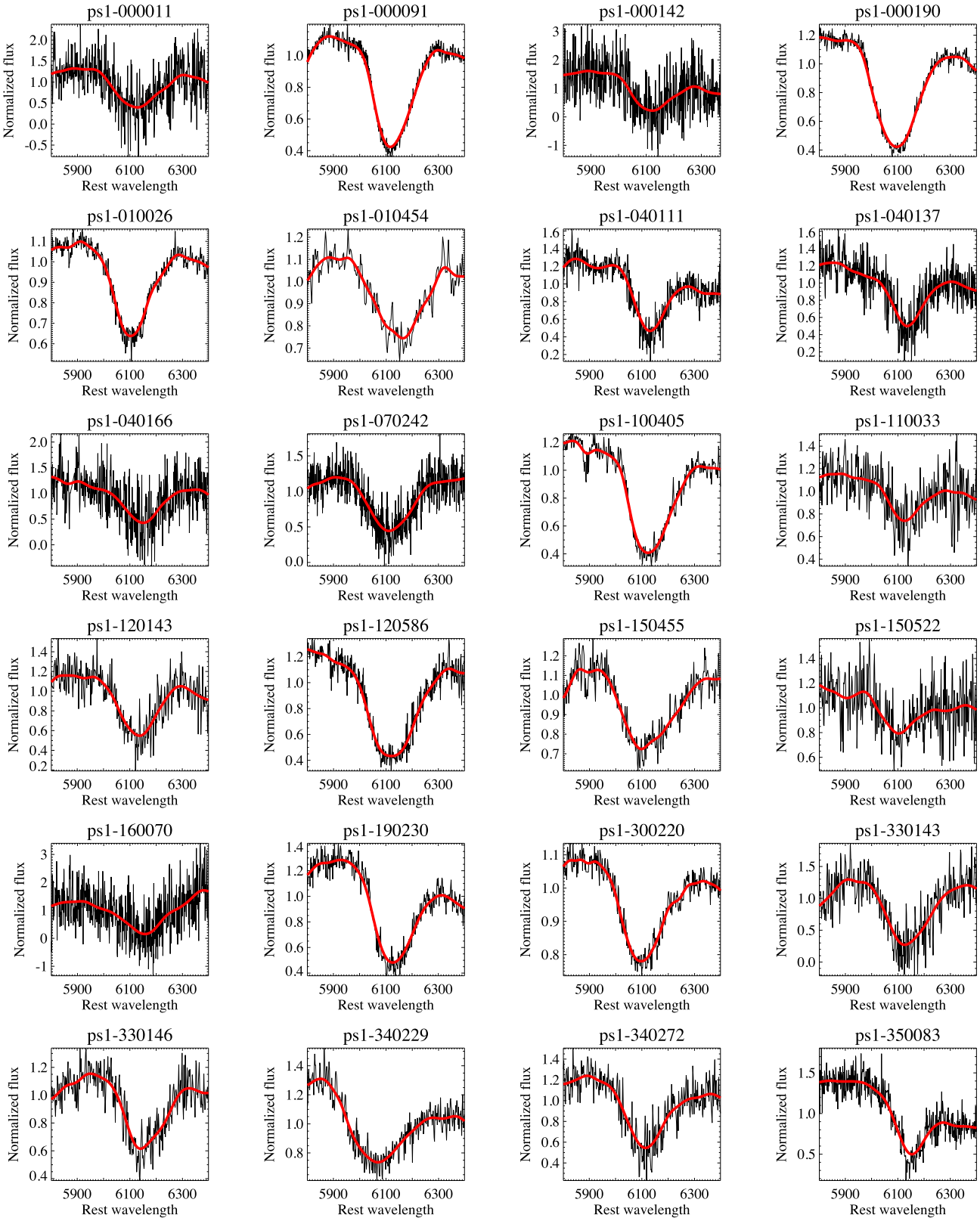

Figure A1. The Si II λ6355 absorption feature measured in this work. The observed and smoothed spectra are shown in black and red, respectively.

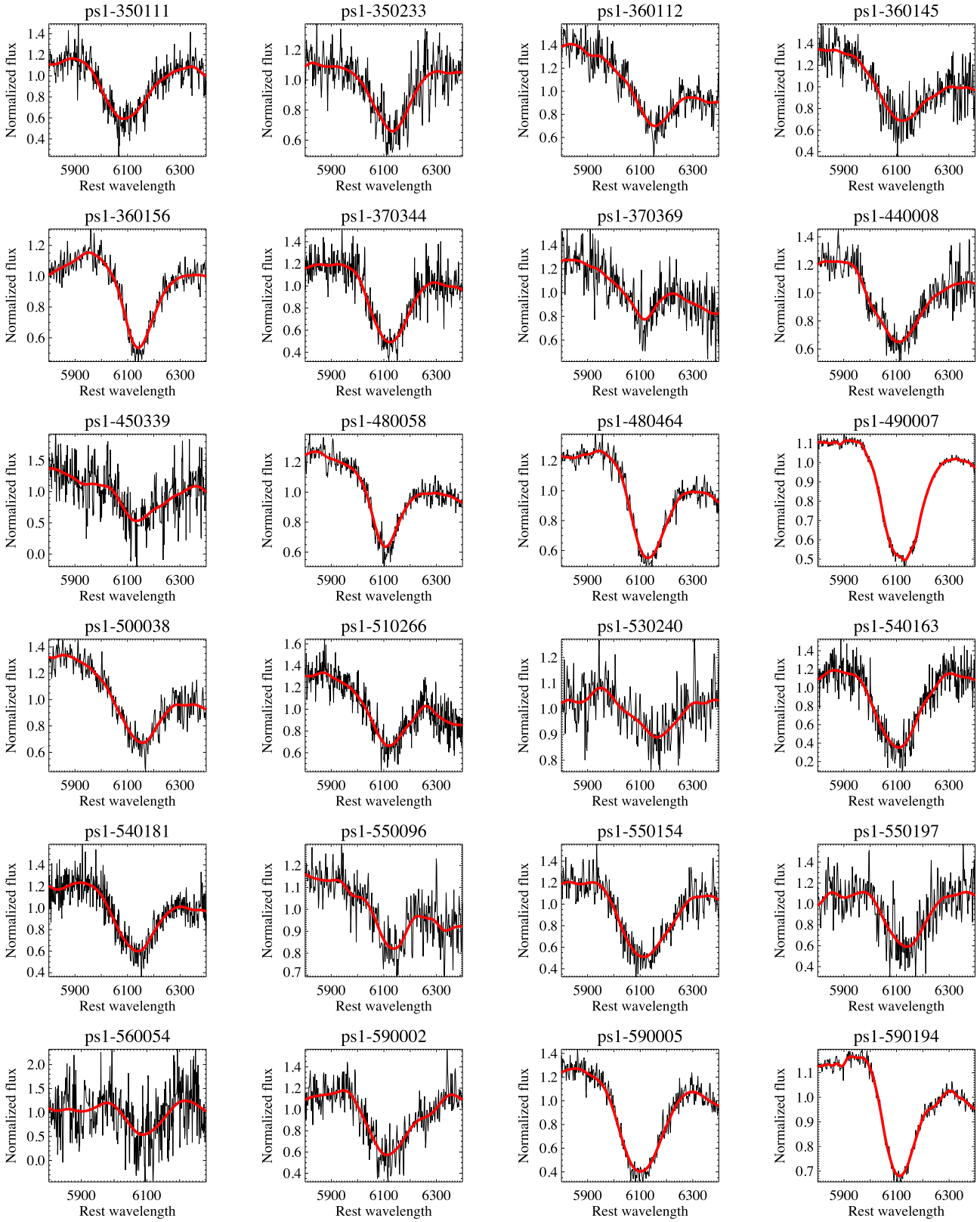

Figure A2. The Si II λ6355 absorption feature measured in this work. The observed and smoothed spectra are shown in black and red, respectively (continued).

APPENDIX B: THE SUMMARY OF $v_{\rm Si\,II}$ MEASUREMENTS IN THIS WORK

Table B1. The Si II λ6355 velocity ($v_{\rm Si\,II}$) measurements of high-z samples (including PS1-MDS, SDSS, and SNLS) used in this work.

SN Name	Redshift (z)	Phase (d)	$v_{\rm Si\,II}$ ($\rm km\,s^{-1}$)	$\sigma_{v_{\rm Si\,II}}$ ($\rm km\,s^{-1}$)
PS1-000011	0.381	2.7	−10633	128
PS1-000091	0.153	2.7	−11265	47
PS1-000142	0.437	1.6	−11048	151
PS1-000190	0.102	−2.6	−12232	19
PS1-010026	0.032	−3.4	−11831	28
PS1-010454	0.081	2.0	−9048	55
PS1-040111	0.370	4.3	−10609	40
PS1-040137	0.447	2.8	−10298	214
PS1-040166	0.440	3.5	−9515	82
PS1-070242	0.064	−4.5	−11473	51
PS1-100405	0.103	4.8	−10907	69
PS1-110033	0.205	−3.5	−10836	45
PS1-120143	0.174	3.2	−10152	19
PS1-120586	0.230	0.9	−11039	58
PS1-150455	0.064	−0.4	−12157	44
PS1-150522	0.230	2.3	−11878	68
PS1-160070	0.359	3.2	−9491	171
PS1-190230	0.139	2.3	−10760	40
PS1-300220	0.094	−3.2	−12329	132
PS1-330143	0.187	0.8	−10600	265
PS1-330146	0.135	1.4	−10223	92
PS1-340229	0.141	4.7	−13459	19
PS1-340272	0.195	−0.9	−11595	194
PS1-350083	0.368	4.7	−9496	113
PS1-350111	0.253	2.4	−12841	215
PS1-350233	0.169	−3.6	−10435	126
PS1-360112	0.181	−0.5	−9388	96
PS1-360145	0.199	4.9	−11020	314
PS1-360156	0.046	−4.0	−10147	14
PS1-370344	0.331	2.9	−10923	89
PS1-370369	0.191	4.1	−11223	17
PS1-440008	0.147	−1.6	−11617	23
PS1-450339	0.410	−0.5	−10359	42
PS1-480058	0.034	4.9	−11739	28
PS1-480464	0.221	−1.1	−10638	15
PS1-490007	0.055	0.8	−11525	21
PS1-500038	0.107	4.7	−9307	130
PS1-510266	0.440	−3.4	−11072	76
PS1-530240	0.117	−0.2	−9015	51
PS1-540163	0.330	−4.6	−11619	56
PS1-540181	0.309	−4.7	−10199	93
PS1-550096	0.225	−4.2	−10209	164
PS1-550154	0.210	−1.3	−11397	199
PS1-550197	0.248	3.6	−10175	130
PS1-560054	0.480	−0.2	−12553	206
PS1-590002	0.199	−1.4	−11473	68
PS1-590005	0.171	0.2	−11978	28
PS1-590194	0.090	−1.8	−11463	15
SDSS2372	0.181	2.1	−11795	197
SDSS2561	0.118	0.0	−9492	229
SDSS2789	0.290	3.9	−9097	151
SDSS2916	0.124	1.2	−10509	53
SDSS3080	0.174	−4.5	−9623	189
SDSS3592	0.087	0.2	−10861	84
SDSS5533	0.220	2.3	−10199	34
SDSS5549	0.121	0.3	−10512	174
SDSS6057	0.067	3.4	−11469	249
SDSS6315	0.267	2.7	−13058	44
SDSS6699	0.311	3.7	−10450	86
SDSS6933	0.213	0.4	−11089	52
SDSS6936	0.181	−0.3	−10077	121
SDSS7147	0.110	0.4	−10503	37
SDSS7475	0.322	3.1	−9384	68
SDSS7847	0.212	−1.4	−14476	63
SDSS10434	0.104	2.5	−9785	202
04D1dc	0.211	−1.7	−10911	155
04D3nh	0.340	4.5	−11778	221
05D2ab	0.323	−1.3	−11072	65
05D2ah	0.184	−2.1	−10951	98
05D3ne	0.169	−4.0	−10987	110
06D3fp	0.268	−0.1	−11779	90

This paper has been typeset from a TEX/LATEX file prepared by the author.